WILEY VCH

Energy Technology
Generation, Conversion, Storage, Distribution

RESEARCH ARTICLE

Ink Processing and its Influence on Particle Size Distribution, Ionomer Requirements and Electrode Properties in Polymer Electrolyte Membrane Fuel Cell and Electrolyzer Catalyst Coated Membranes

Philipp Quarz | Nadine Zimmerer | Linus Janning | Anna-Maria Steck | Philip Scharfer | Wilhelm Schabel

Thin Film Technology (TFT), Karlsruhe Institute of Technology (KIT), Karlsruhe, Germany

Correspondence: Philipp Quarz (philipp.quarz@kit.edu)

Received: 25 August 2025 | **Revised:** 26 September 2025 | **Accepted:** 4 October 2025

Keywords: ball milling | catalyst coated membranes processing | crack area | I/C ratio | membrane direct coating | pore diameter distribution

ABSTRACT

The processing of catalyst-coated membranes (CCM) is a major challenge in the production of efficient fuel cells and electrolyzers. In addition to the material properties and the formulation, the processing of the ink has a decisive effect on the crack pattern of the resulting electrodes. In this work, the influence of milling time in a ball mill on ink and electrode properties is investigated. Prolonged milling results in a reduction in large agglomerates, particularly. The pore diameter distribution of the membrane direct coatings exhibits a strong correlation with the particle size distribution (PSD) of the inks. With regard to the proportion of cracks, an optimum milling time exists. With very long milling time and thus small and narrow PSD, a continuous crack network is created. This phenomenon is explained by the large specific surface area of the dispersed particles and the distribution of the ionomer in the ink. Ionomer adsorbed to the particles is no longer available as a stress-absorbing binder during solidification. A higher ionomer to carbon ratio can compensate for small PSD, enabling low-crack coatings.

1 | Introduction

The catalyst coated membrane (CCM) is the key component of polymer electrolyte membrane (PEM) fuel cells and electrolyzers. The main mass transport processes and electrochemical reactions take place here. The challenges for the two catalyst layers of the CCM are to enable a high mass transfer of the gaseous reactants and products as well as a high catalytic effect. This is achieved by a microstructure with high porosity and defined pore diameter distribution for mass transfer of the gases, many three-phase boundaries around the catalyst and good contact with the proton-conducting membrane and as well a good contact to the electron-conducting porous transport layer [1–4].

The desired microstructure depends on both the materials used and the way in which they are processed. The literature covers a wide range of catalyst particles, ionomers, solvents, and additives and their combinations when selecting ink materials, e.g [5–15]. Conversely, few systematic studies have been conducted on processing. Nevertheless, this field is of significant importance, given that the process route (decal or membrane direct coating) [16, 17] and each step of the process, including ink processing [18–20], coating [17] and drying [21–24], affects the microstructure of the final layer. This study focuses on the influence of processing in a ball mill, an industrially scalable device. A fundamental understanding of the process is required for industrial applications. To this end, the key interrelationships, such as the ionomer

distribution, must be identified and discussed. This study aims to address this research gap.

1.1 | Role of the Ionomer

The composition of the components in the form of the solvent ratio and the ionomer to carbon ratio (*I/C*) has a decisive influence on the ink properties and the microstructure of the resulting electrodes [21, 22, 25–27]. A higher *I/C* reduces the vulnerability to cracking [15]. But, if too high, it can cause the catalyst particle network to clog [28], reduces the size of pores, and thus negatively affects the mass transfer during operation and total CCM performance [1, 29, 30].

The ionomer plays a critical role in providing proton conduction to the membrane during operation and stabilizing the ink during processing [31, 32]. It accumulates on the particles during the grinding and mixing process as an ultrathin film with a thickness of just a few nanometers. The distribution and thickness over the particle surface are heterogenous [12, 28, 33, 34]. Kumano et al. [35, 36]. showed that free ionomer, not adsorbed to the particles, can also be present in an ink, serving as a binder between the particles during film solidification [12, 36–39].

High surface area catalyst particles, for example, Ketjenblack, require more ionomer for stabilization than lower surface area particles, for example, Vulcan XC-72 [32, 39, 40], at the expense of free ionomer [15]. In addition, the thickness of the ionomer film around the particles decreases as the particle size decreases [41].

The distinction between polymer bound or immobilized to the disperse phase (particles or droplets), which sterically and electrostatically stabilizes the particles or droplets in solution, and free polymer, which serves as a binder between the individual particles during film solidification, is also an established explanation for other disperse systems such as battery slurries [42, 43] or oil–water emulsions [44]. When new surfaces are generated, for example, through a break-up of agglomerates, (excess) free ionomer will adsorb to it [44]. Moreover, excess adsorbed ionomer can cause flocculation of the disperse phase [42].

1.2 | Ink Processing in a Ball Mill

Comparing to formulation effects, a systematic investigation of the processing of catalyst inks and its effects on particle size distribution (PSD) and layer's properties has not received as much attention to date. The original agglomerates from the supplied catalyst powder must be broken up and mixed with the other ink components to produce thin film coatings with a high electrochemically active surface area. This is typically achieved using ultrasonication, high-speed mixing, or ball milling [40].

Ball mills and similar systems offer several advantages, incl. simultaneous comminution, and mixing, scalability for large-scale production, and the production of high-quality inks [18], as far as the authors know, without loss of platinum from the particles.

Several process parameters effect the ball-milling result [19, 45, 46]. Combined, two main parameters for particle size reduction can be derived from literature articles: the stress intensity **SI** (Equation (1)) and the stress number **SN** (Equation (3)) [47].

SI describes the energy exerted on the process side, which must be larger than the material-specific required comminution energy. It is approx. proportional to the kinetic energy of the grinding media (GM) SI_{GM} and depends on its diameter d_{GM}, density ρ_{GM}, and speed v_{GM}, which in turn is proportional to the diameter of the grinding disk d_{GD} and the rotational speed n (Equation (2)).

$$SI \propto SI_{GM} = {d_{GM}}^3 \cdot \rho_{GM} \cdot {v_{GM}}^2 \tag{1}$$

$$v_{GM} = \pi \cdot d_{GD} \cdot n \tag{2}$$

SN is described as the average number of stress events of a particle or agglomerate in a batch milling process. In the model equation, it is determined by the filling ratio φ_{GM}, and the porosity of the bulk of GM ε, the volumetric solid content of the product suspension Φ_v, and GM's diameter d_{GM}. Furthermore, the rotational speed $\boldsymbol{n}$ and the grinding time $\boldsymbol{t}$ are also included linearly.

$$SN \propto \frac{\varphi_{GM} \cdot (1-\varepsilon)}{(1-\varphi_{GM} \cdot (1-\varepsilon)) \cdot \Phi_v} \cdot \frac{n \cdot t}{d_{GM}} \tag{3}$$

The process parameters can be optimized for specific material systems [46]. Regarding the SN, it can be hypothesized that a longer milling time leads to multiple stress events and consequently to smaller particle sizes. This has already been shown qualitatively for fuel cell inks by Lindermeir et al. [19]., Baez-Cotto et al. [18], and Liu et al. [20].

Furthermore, the PSD of a catalyst ink influences the microstructure of the catalyst layers. One related layer property is the pore diameter distribution [48]. Going further, the pore diameter distribution affects the cell performance [11]. The initial agglomerates possess internal porosity, and their disruption affects the resulting ionomer network, electrochemical active surface area, and performance [49].

1.3 | Formation of Electrode Cracks

Another issue affecting (long-term) cell performance is cracks in the catalyst layers. Although their influence is not fully understood, it is known that they can have both positive and negative effects. During operation, cracks can facilitate mass transport of the reactants [50, 51]. However, they can also cause interruptions in conductivity and mechanical weak spots in the system [52–55]. In consequence, cracks are also detrimental to the CCM durability [56]. The general consensus in the literature is to avoid cracks.

Cracks can occur during the electrode drying in CCM production due to stresses during film solidifying [23, 57, 58]. Nucleation points may be present in film inhomogeneities, for example, large agglomerates [9, 36]. Furthermore, there is a critical layer thickness, the critical crack thickness (CCT), above which individual cracks spontaneously occur [58]. The CCT is a function of the stress generated within the solidifying film and the mechanical properties of the film, which corresponds to the resistance to fracture, influenced by several material-specific parameters [58–61]. For porous films with hard particles, one factor influencing crack

formation is the size of the involved particles. Smaller particles result in a lower CCT. This can be explained by the fact that a smaller particle size leads to a smaller pore width, thus to an increase in capillary pressure and higher stresses in the porous system [58, 60].

PSDs show increasingly inhomogeneous stress behavior in thin films [62]. Wider PSDs exhibit higher stresses due to higher particle packing densities, smaller pores, and consequently higher capillary pressures. To increase the mechanical stability of a layer, however, additives like polymeric binders [61, 63] or carbon nano tubes (CNT) [9] can be added.

Beyond that, the manufacturing process has an influence on the CCT and cracking. Changes in the solvent composition due to selective solvent evaporation affect surface tensions, ionomer and particle properties, and consequently cracking [22]. The CCT and crack patterns are also influenced by the choice of the substrate. In addition to all the theoretical influences, the product-related required or desired film thickness is also decisive. In general, higher layer thicknesses lead to more pronounced crack patterns in fuel cell catalyst layers. However, these also depend to a large extent on the specific materials used [9, 15, 21].

Since in this study, the processing of catalyst inks is investigated, particle size (distributions), shapes, and thus packing densities in the film change. The influence of these changes on the crack formation in catalyst layers is also a focus of this study to further understand cracking of complex catalyst films.

2 | Material and Methods

2.1 | Ink Production

Catalyst powder TEC10EA50E with 46 wt% platinum (TANAKA Kikinzoku Kogyo K.K., Japan) was mixed with Nafion D2020 (Chemours, USA), 1-propanol (Carl Roth GmbH, Germany) and ultrapure water (Milli-Q EQ (7000), Merck, Germany). The solid content was set to 10 wt% and the gravimetric ionomer to carbon ratio (I/C) varied between 1.0, 1.2 and 1.5. I/C of 1.0 is frequently used in the literature, for example, [5, 18]. 1.2 and 1.5 result from considerations regarding the particle surface in the course of the study. The overall ratio of 1-propanol to water was 20:80 wt%. Each 30 ml ink was produced in a ball-mill CN 10, APS 250 (VMA Getzmann GmbH, Germany) containing 30 ml GM made of yttrium stabilized zirconium oxide (d_{GM} = 0.6–0.8 mm). Milling time varied for the different inks at a constant speed of 1000 rpm (Table 1 ink A-D). Inks E and F differed in their I/C ratio. For all inks the resulting stress number and stress intensity during the milling process were calculated with Equations (1)–(3) and are given in Table 1.

2.2 | Ink Characterization

PSDs of the inks were determined by dynamic light scattering (DLS) (Mastersizer 3000, Malvern Panalytical, UK). The refractive index of carbon black as main component (n_{CB} = 1.746 [27]) was assumed for the particles. Platinum and ionomer could influence the refractive index. This would cause the curves to shift slightly. Nevertheless, a qualitative comparability is given and measured values are in the expected range. Inks were diluted (∼1:10 000) in an ultrasonically degassed solvent mixture ($n_{solvent}$ = 1.34) with a 1-propanol to water ratio of 20:80 wt%.

TABLE 1 | Process parameters while ink formulation (A-F) in a ball mill.

	t	n	SN	SI_{GM}	I/C
	h	rpm	10^8 m^{-1}	10^{-8} J	g g^{-1}
A	1	1000	1.11	1.14	1.0
B	3	1000	3.34	1.14	1.0
C	6	1000	6.68	1.14	1.0
D	24	1000	26.7	1.14	1.0
E	24	1000	26.7	1.14	1.2
F	24	1000	26.7	1.14	1.5

Note: With increasing grinding time t, the stress number **SN** increases. Additionally, the ionomer to carbon ratio I/C, the rotation speed n and the resulting stress intensity of the GM SI_{GM} are given.

2.3 | Coating and Drying of the Electrodes

Further processing was identical for all inks. The inks were applied directly onto a Nafion N212 membrane (Chemours, USA) using a ZUA 2000 doctor blade (Zehntner-Testing-Instruments, Switzerland). The catalyst film was dried with a combination of contact drying and convective drying, leading to isothermal drying conditions. The isothermal drying temperature was set to 25°C and the heat and correlated mass transfer coefficient was set constant in the dryer to a fixed value of 35 W m^{-2} K^{-1}. This results in calculated mass transfer coefficients of 0.018 m s^{-1} for 1-propanol and 0.030 m s^{-1} for water into the drying air. The relative humidity of the drying air was between 10% and 24% at 25°C. With the solvent composition used in the inks, this had no relevant effect on the drying behavior [22].

2.4 | Analysis of the Catalyst Layers

The film thickness was determined using a digital dial gauge (ID-H0530, Mitutoyo, Japan). A digital microscope VHX-7000 (Keyence, Japan) was used for microscope images. Cracks were studied by backlight images of the layers and analyzed using an automated in-house machine learning software. The pore size distribution was determined using mercury intrusion (Poremaster GT33, Anton Paar, Austria).

3 | Results and Discussion

3.1 | Influence of the Milling Time on the Particle Size Distribution

The material source for the catalyst inks is the powder of the catalyst particles. These are initially present as agglomerates with mean diameters in the range up to ≈80 µm (see Figure S1,

Supporting Information), which must be broken up in a grinding step.

Figure 1 shows the volumetric PSD of inks milled for 1, 3, 6, and 24 h at a rotation speed of 1000 rpm. All inks milled for 1 to 6 h show a bimodal PSD. The inks were diluted for characterization. The error bars result from measurements of different samples of the particular ink.

The fine fraction in the PSD is less than ≈100 nm and refers to the primary particles and smallest aggregates. The coarse fraction larger than 100 nm refers to aggregates and bigger agglomerates. The largest agglomerates measured in the milled inks are significantly smaller than in the unmilled powder (t = 0 h).

The peak in the coarse fraction shifts to smaller particle sizes with longer milling times. Simultaneously, the fine fraction peak rises. The transition to the fine fraction is fluent in the ink that has been milled for 24 h (green). Longer mixing and grinding in the ball mill leads, as expected, to a more narrow PSD.

Theoretically, this can be explained by the higher impact number *SN*. *SN* increases with the grinding time and rises the chance of agglomerate break-ups (see Equation (3)). Starting from large catalyst agglomerates, via smaller aggregates, finely dispersed primary particles are produced. The SI resulting from the setup is high enough to break up the agglomerates and aggregates (see Equation (1)).

For all percentile values, the corresponding size values are observed to be smaller with longer milling times (Table 2). The corresponding cumulative PSD resulting from Figure 1 shown in the Figure S2, Supporting Information. The x_{10} values of the processed inks, which represent the smallest size fractions,

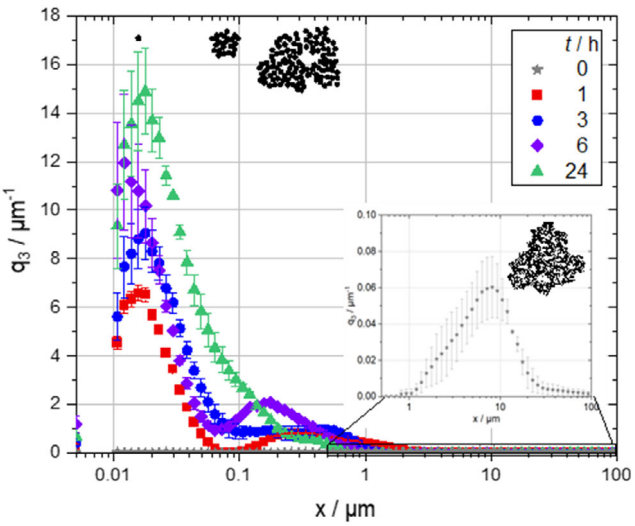

FIGURE 1 | PSD depending on ink milling time from t = 1, 3, 6, and 24 h in a ball mill with constant rotation speed of 1000 rpm. The schematic representation above depicts the primary particles, aggregates and larger agglomerates, anticipated for each size class. In addition, the PSD of the catalyst powder in the solvent mixture without further processing (t = 0 h) with large agglomerates is shown in a zoom between 0.5 and 100 µm.

TABLE 2 | x_{10}, x_{50}, x_{90} and x_{99} of the PSDs of inks milled to varying lengths.

	0 h[a]	1 h	3 h	6 h	24 h
x_{10}/µm	4.6	0.03	0.02	0.02	0.02
x_{50}/µm	11.7	0.63	0.34	0.20	0.07
x_{90}/µm	61.3	1.77	0.83	0.57	0.37
x_{99}/µm	105	2.60	1.13	0.94	0.61

[a]0 h represents catalyst particles in the solvent mixture without ionomer and without milling.

are in a narrow range for all curves (0.02 to 0.03 µm). Larger differences can be seen in the x_{50} and x_{90} (Table 2). Longer milling reduces the size of the largest agglomerates in particular.

The maximum detected particle size also decreases with increasing grinding time. After 1 h of milling, the largest agglomerates previously present in the catalyst powder are two orders of magnitude smaller. While 2.6 µm-large particles are still present as x_{99} after 1 h, the x_{99} is 1.1 µm after 3 h, 0.9 µm after 6 h and 0.6 µm after 24 h. This is important to note regarding the potential for cracking in films produced with these inks, as larger agglomerates can act as starting points for cracks and other defects [9, 36].

It should be noted that when measuring particle sizes using DLS, the ink sample is strongly diluted (≈1:10 000). This could and will influence the PSD. Measured size values could differ from those actually present in the ink. For example, in the case of carbon black in isopropanol, a 20% reduction in particle size was observed at a dilution of 1:100 [31]. However, the order of magnitude should be similar, and the qualitative comparison of the samples is justified due to matching expected primary particle sizes and same effects for every measurement. In general, DLS is a frequently used analysis method for ink characterization [40, 31]. In contrast, pure ionomer aggregates are only a few nanometers in size [64], and therefore cannot be detected by the DLS system used, which has a lower detection limit of 10 nm. To minimize the influence of technical effects, the inks were always diluted and measured in the same way. This leads to the initially uncheckable assumption that the dilution for particle size determination has no effect on qualitative statements of the inks relative to each other. This must be taken into account when discussing the results.

3.2 | Influence of Milling Time and Stress Number on the Crack Pattern

The inks were applied directly onto a Nafion N212 membrane under comparable coating and drying conditions, resulting in an average dry layer thickness of 7.4 ± 0.5 µm. This corresponds to a calculated platinum area loading of ≈0.17 ± 0.02 mg cm^{-2}. Any differences in the electrodes are solely attributed to the specific characteristics of the inks.

In Figure 2, defects and cracks in the layers are visible as white spots, since the pictures are taken with backlight.

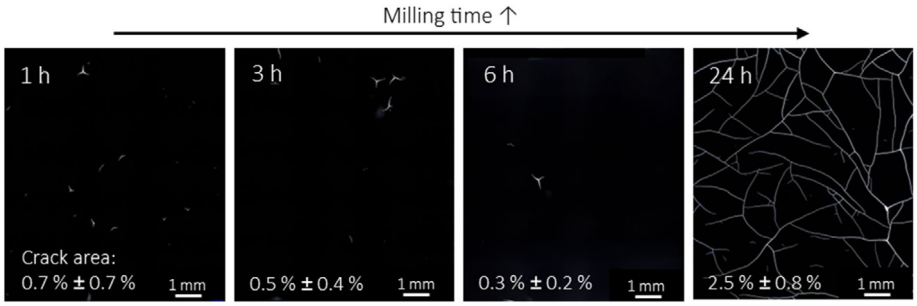

FIGURE 2 | Observed surface of catalyst layers with cracks after different ink milling times of 1, 3, 6, and 24 h. All inks were directly coated onto the membrane and dried under similar drying conditions. The dry layer thickness of all layers is around 7.4 ± 0.5 μm. The number of cracks and the proportion of cracks observed in the dry layers initially decrease with longer milling times. However, if the milling time is too long, a crack network is formed. Defect area fraction compared to total area is given.

The layers from inks prepared with milling times of 1–6 h show mostly small and short cracks. The crack form and size do not change significantly regardless of the milling time in contrast to [18] and most can be classified as Y-shaped cracks, randomly oriented [36]. Most cracks start at inhomogeneities, such as agglomerates (see Figure S3, Supporting Information).

With increasing milling time, the crack area of the layers relative to the total layer area initially decreases slightly from 0.73% (1 h) via 0.48% (3 h) to 0.25% (6 h) (Figure 3).

The layer of the ink processed for 24 h has a very pronounced and interconnected crack network. In the layer, some larger, delaminated areas are visible. These are likely the result of delamination and spalling of individual layer islands, which were bordered by cracks. The overall crack proportion in the catalyst layer with the ink milled for 24 h is 2.5%. The crack area is more than ten times higher than the relative defect area after 6 h milling time. Reasons for the differences in the crack network are discussed subsequently.

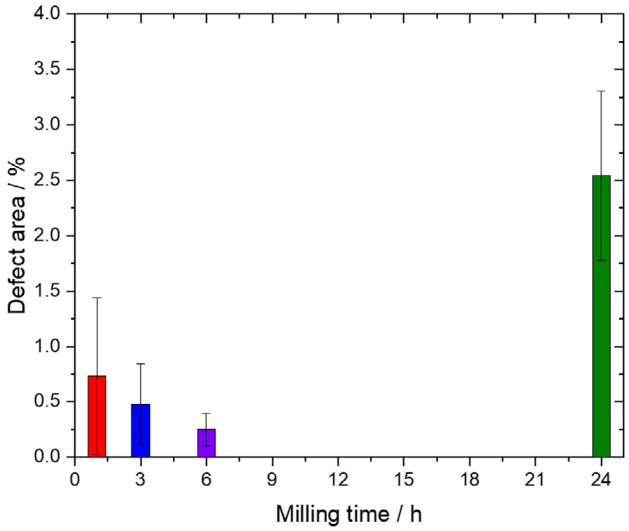

FIGURE 3 | Percentage of defect area (cracks, spalling, etc.) relative to the total area of the membrane direct coatings over the ink milling time. Inks were milled for 1, 3, 6 and 24 h. Subsequently, all films were dried equally at an isothermal film temperature of 25°C with gas phase mass transport boundary conditions corresponding to a heat transfer coefficient of 35 W m^{-2} K^{-1}.

3.3 | Influence of Milling Time on the Pore Diameter Distribution

In the following, the layers are analyzed in more detail. The pore diameter distribution is an important microstructure parameter and is the subject of the following investigations (Figure 4).

The limitation of the measuring device restricts the resolution to a minimum pore size of ≈6 nm. Any internal pores in porous primary particles themselves are expected to be smaller than the measurement resolution. As the same catalyst material was used for all the inks analyzed, the internal pores of the primary particles should always be similar in size and frequency, but were not detectable in this case. The smallest measurable pores could possibly occur as primary pores within the individual agglomerates and aggregates. In addition, the larger pores are initially interpreted as secondary pores between different agglomerates.

The maximum pore size found is <0.1 μm. As the grinding time increases, the pore diameter distribution shifts toward smaller

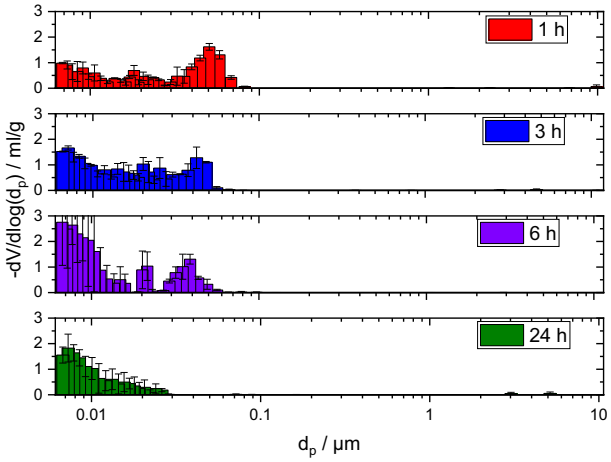

FIGURE 4 | Influence of the ink milling time of 1, 3, 6, and 24 h on the pore diameter distribution in the final dried electrodes shown in Figure 2.

pore diameters d_p. The number of small pores increases slightly, while the number of large pores decreases. The greatest amount of very small pores ($d_p < 0.02$ µm) is observed after 6 h of milling. The largest significant pore size also becomes smaller. This is consistent with the PSD (see Figure S4, Supporting Information), as the $\boldsymbol{x_{10}}$ are pretty similar for all milling times, but mainly the larger particle sizes are reduced (see Table 2).

A bimodal pore diameter distribution can be seen in the layers from all inks except for the layer from the ink processed for 24 h. This is similar to the course of the corresponding PSD. The highest proportion of smallest pores is recorded after 6 h. After 24 h, fewer of the smallest pores are present than after 6 h.

Pore size correlates with particle size, shown in the experiments here and the literature. This refers initially to the secondary pores [48]. However, a larger agglomerate is also expected to have larger primary pores than a smaller agglomerate (see Figure S5, Supporting Information). When the large agglomerates are broken, both the large secondary pores and the large primary pores decrease. Overall, the amount of larger pores decreases.

Theory argues that cracks result from high capillary pressures exceeding a certain cohesion value of the film [58, 60]. That is why the critical crack thickness is reduced with high capillary pressures resulting from small pores. Subsequently, given that the proportion of smallest pores is observed to be the highest for the films made from inks that were milled for 6 h, it is anticipated that the greatest number of cracks would be present here. However, the opposite is observed, with the fewest cracks occurring in the film from the 6 h-ink. The capillary pressure alone is not sufficient to explain the observed cracking behavior. Rather, the cohesion in the layers must change as the resistance to capillary pressure induced stresses in order to explain the observed behavior. If the cohesion decreases, cracks will occur at some point at (nearly constant) capillary pressures. This is presumably linked to the ionomer (distribution).

3.4 | Effect of Particle Size Distribution on the Ionomer Distribution in Ink and Layer

When agglomerates are broken up into smaller primary particles, the specific surface area S_V, which is the ratio of surface area to volume, increases (Equation (4)). For perfectly assumed spheres with a diameter of x, this ratio can be exactly calculated [65]:

$$S_V = \frac{6}{x} \tag{4}$$

The grinding of particles results in a larger effective particle surface area, which must be stabilized to avoid re-agglomeration. More ionomer is required. If the *I/C* ratio and the catalyst particle mass m_C resp. volume in the ink remain constant, there may not be enough ionomer available to sufficiently cover the surface of the particles obtained during ink processing for stable particle dispersion.

This is shown schematically in Figure 5 for the inks after 1, 3, 6, and 24 h of milling. The measured x_{50} (see Table 2) from experimental ink investigation serve as the respective particle size. An agglomerate with $x_{50} = 0.63$ µm present after 1 h of ink processing is broken into multiple smaller agglomerates with a size of 0.2 µm after 3 h of ink processing. These, in turn, are broken into numerous even smaller aggregates and primary particles as the milling time continues.

The newly created surface can or must be covered by ionomer in equilibrium. For this purpose, the initially free ionomer adsorbs onto the new surface. If the surface area is too large, there will eventually be no more free ionomer in the liquid phase in-between the particles. Further particle adsorption is not possible. Since the ionomer also acts as a stabilizer, the small particles will (over time) re-agglomerate.

To quantify the increase of particle surface, as an approximation, the number of particles can be calculated assuming that the

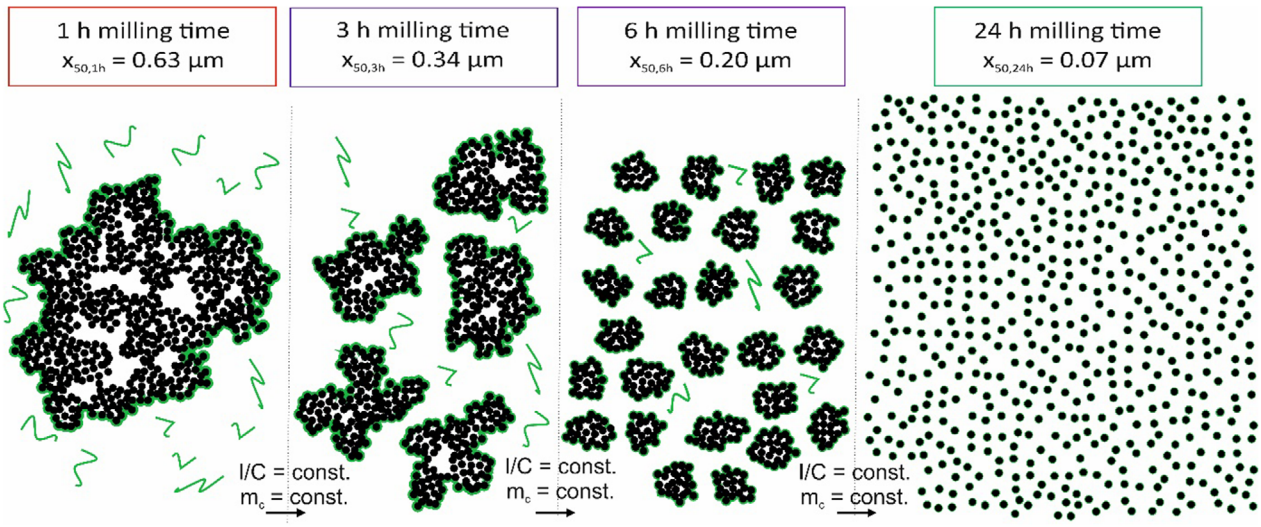

FIGURE 5 | Schematic illustration of the influence of the milling time $\boldsymbol{t}$ on the number n and size $\boldsymbol{x_{50}}$ of agglomerates, aggregates and primary particles and their specific surface area $\boldsymbol{S_V}$. The stated size per milling time corresponds to the $\boldsymbol{x_{50}}$ of the experimentally tested inks. Taking a constant ionomer to carbon ratio *I/C* and catalyst content m_C, with increasing milling time the size of particles decreases and their number and specific surface area increase. More ionomer adsorbs at the greater surface and the content of free ionomer in solution decreases.

agglomerates are nonporous and monomodal (Equation (5)). If the total particle volume remains constant, the number of particles N_i can be calculated as follows. A large sphere is split into several smaller spheres, the total volume of which is exactly the same as that of the original sphere. Due to this volume connection, the size ratio is incorporated into the number ratio cubically [65].

$$\frac{N_2}{N_1} = \left(\frac{x_1}{x_2}\right)^3 \tag{5}$$

Thus (for non-porous particles) one single particle with a diameter of 0.63 µm at 1 h milling time would become six with a diameter of 0.34 µm at 3 h milling time, 31 with 0.20 µm at 6 h milling time and 729 with 0.07 µm at 24 h milling time. Since the specific surface area is inversely proportional to the particle size and resulting from Equation (4), S_V increases by a factor of 1.9, 3.2 and 9.0. The values serve as a conservative estimation.

The assumption of non-porous particles is a simplification for estimating upper limits for the number of primary particles and specific surface areas. In reality, the large particles are actually porous agglomerates and aggregates of primary particles and intermediate voids. Assuming an internal agglomerate porosity of 40%, the number of primary particles and thus the total specific surface area of the primary particles formed from the large agglomerate would be correspondingly reduced by 40% [65].

The effective surface area of an agglomerate or aggregate for ionomer adsorption can be described by the outer surface. Due to very small internal pores, no or less ionomer is to be expected within an aggregate or agglomerate.

In any case, the aforementioned effects also apply to aggregates and agglomerates with internal porosity formed from primary particles. The many smaller particles have a larger surface area than the aggregates and agglomerates, which results in a greater adsorption of ionomer. Consequently, the concentration of free ionomer in the ink decreases.

3.5 | Free Ionomer as Crack-Resistant Binder

The total amount of ionomer $m_{I,total}$ in an ink is set by the formulation. However, the ionomer (I) is present in different forms within the ink [35, 36]:

- free ionomer: free in solution and postulated to act as binder between particles during film solidification (index: binder);
- adsorbed and immobilized ionomer on the primary particle or agglomerate surface (index: surface);
- immobilized ionomer within porous agglomerates or porous primary particles (e.g., Ketjenblack) (index: porosity).

The proportions may vary depending on the manner in which the ink is processed, but the total quantity remains constant (Equation (6)). The individual masses of the different ionomer forms can be expressed by their volume and the corresponding density (Equation (7)).

$$m_{I,total} = \text{constant} = m_{I,binder} + m_{I,surface} + m_{I,porosity} \tag{6}$$

$$m_{I,total} = \rho_{I,binder} \cdot V_{I,binder} + \rho_{I,surface} \cdot V_{I,surface} + \rho_{I,porosity} \cdot V_{I,porosity} \tag{7}$$

The volume of ionomer $V_{I,binder}$ that is freely available in the ink and is suitable for the formation of low-crack to crack-free layers is the residue that remains in the ink when the adsorbed portions are subtracted from the overall ionomer volume.

The densities of the individual ionomer modifications differ due to the interactions with the immediate environment. The density of the free ionomer $\rho_{I,binder}$ depends on the properties and interactions with the surrounding solvents [64]. Further, the density of the adsorbed ionomer $\rho_{I,surface}$ is effected by the solvents and the particle surface (e.g., platinum content) and for the ionomer within the agglomerates and porous primary particles $\rho_{I,porosity}$, the interactions within the agglomerate and particle microstructure are relevant [32, 66]. Changing conditions during ink application and drying may alter these interactions.

The term for $V_{I,surface}$ can be more precisely defined under two premises (Equation (8)):

- the ionomer adsorbs onto (the newly formed) agglomerate or primary particle surface and is in equilibrium with it and
- spherical particles are present.

The amount of adsorbed ionomer is calculated from the sum of all volumes of a spherical shell of shell thickness d around each of the n_i particles with size x_i of all size classes. In the factor ξ, potential incomplete surface coverage and geometric deviations are taken into account.

For $x_i \gg d$, the term can be simplified by using the sphere surface times the shell thickness (Equation (9)). For a constant shell thickness, independent of the particle size, even the explicit conversion of Equations (9) and (7) to d would be possible. Simplified and summarized, the free ionomer content in the ink is a function of the PSD (Equation (10)).

$$V_{I,surface} = \sum N_i \cdot \xi \cdot \frac{\pi}{6} \cdot ((x_i + 2d)^3 - {x_i}^3) \tag{8}$$

$$V_{I,surface} \approx \sum N_i \cdot \xi \cdot \pi \cdot {x_i}^2 \cdot d \tag{9}$$

$$V_{I,binder} = f(\text{PSD}) \tag{10}$$

In the milling process, if new surface is created while the agglomerates and aggregates are broken up, the amount of free ionomer will decrease (see Figure 5). If there is no free ionomer available anymore to compensate for the newly created particle surface, there are theoretically two consequences for the ionomer adsorption on the particle:

- (I) The shell thickness around the individual particles decreases (Figure 6i). This is also described in [41]. This could be at the expense of particle stabilization and may no longer actively prevent re-agglomeration.

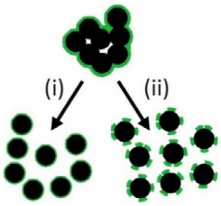

FIGURE 6 | Effect of the particle surface area on the ionomer shell around particles. If no additional free ionomer is available from the ink, (i) the ionomer shell thickness must become thinner or (ii) the particles are only partially covered with increasing surface area.

- (II) The surface loading of the ionomer can be reduced, which will then be partially covered by the ionomer (Figure 6ii). This could also reduce particle stabilization.

3.6 | Higher I/C Ratio for Compensating Large Specific Particle Surface Area

The hypothesis that free ionomer is required to prevent cracking is tested for plausibility with a higher *I/C* ratio. If the most of the ionomer is adsorbed on the particle surface, the proportion of free ionomer can be enhanced by the addition of more ionomer. Since the layer pattern looks best after 6 h, it is assumed that there is enough free ionomer available for the given PSD. The *I/C* of 1.0 matches the present PSD in this ink. Different for 24 h of grinding, where the layer pattern is cracked and the *I/C* ratio is interpreted as too low for the given PSD. The amount of ionomer required to cover the particle surface and have excess free ionomer for a crack-free layer pattern can be estimated by calculating the total specific surface area of the respective inks from their PSD. The ratio of the simplified estimated specific surface areas per gram of printing ink D (24 h) to C (6 h) is 1.42. Therefore, inks with increased *I/C*, once with less than this factor (Ink E $I/C = 1.2$) and once with slightly more (Ink F $I/C = 1.5$) were produced experimentally, milled for 24 h and compared with the original Ink D with $I/C = 1.0$.

Regarding the PSD of the inks, all three inks milled for 24 h, but different *I/C* ratio, show a very similar distribution (Figure 7). In the tested range, the *I/C* seems to have no significant influence on the resulting PSD. Similar observations were made by Hoffmann et al. [15]. Based on these results, it can be assumed that all three inks effectively exhibit a similar surface area that has been wetted with ionomer.

In the next step, the layers produced from the inks are analyzed in more detail. At higher *I/C*, fewer (larger) pores are measured (see Figure S6, Supporting Information). The ionomer seems to constrict and close the pores during film formation. This may be due to a thicker ionomer shell around the particles or due to ionomer still present as free ionomer in the liquid ink, which then binds the particles in the layer. Similar observations have been made by [1, 30].

Comparing the crack patterns, a crack network can still be seen at $I/C = 1.2$ (Figure 8). However, the network is less dense (2.3% ± 0.8%). A clear improvement in the layer pattern in the form of a smaller total defect area can be observed when

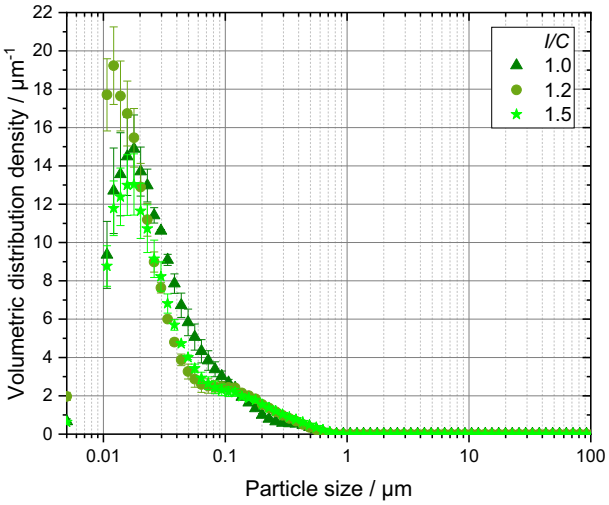

FIGURE 7 | PSD depending on the *I/C* ratio (1.0, 1.2 and 1.5) for inks milled for 24 h at 1000 rpm.

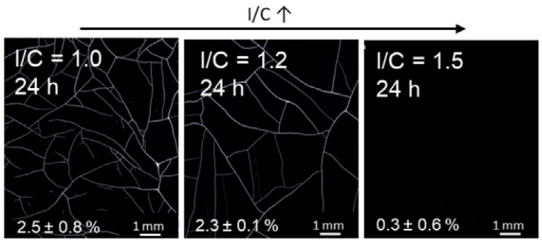

FIGURE 8 | Catalyst layer pattern depending on the *I/C* ratio. The inks were all milled for 24 h, directly coated onto the membrane and dried comparably. Layer thickness is comparable.

additional ionomer is added. With $I/C = 1.5$, the crack area fraction is 0.3% ± 0.6%. This is explained due to free ionomer in the ink acting as a binder between the particles during solidification.

A slight improvement in the film appearance can also be seen in films with only single defects ($I/C = 1.2$–1.0 after 3 h of milling and comparable PSD, see Figures S7 and S8, Supporting Information). The positive effect is less pronounced in this case, because the original layer already had a smaller crack area.

The hypothesis of free ionomer, which can be introduced into the ink by adding ionomer to compensate for large particle surfaces in order to stabilize the films against cracking, is further confirmed. The beneficial quantity of ionomer and the surface area of the particles are coupled. The quantity of free ionomer is of particular importance, as it has a positive effect on the crack resistance of the layer but may clog the pores.

It should be noted that the aim of this study is to improve the film appearance and to discuss the fundamental effects of ink processing. Optimized system performance during operation does not necessarily correlate with this. The break-up of large agglomerates affects a number of overlapping factors, including the increase in electrochemically relevant three-phase-boundaries, particle wetting with ionomer, proton conductivity, pore size, overall porosity and crack pattern.

4 | Conclusion

Catalyst inks were processed for different milling times and directly coated onto a Nafion N212 membrane with doctor blade coating. Longer milling times lead to more small particles and a more narrow PSD. This is accompanied by a similar trend in the pore diameter distributions of the electrodes produced from these inks. The reduction in particle size resulting from longer ink processing leads to a concomitant reduction in layer pore size.

For a given ionomer to carbon (*I/C*) ratio, there is an optimum milling time for minimum crack area. The crack area initially decreases with grinding time. This is explained by fewer large agglomerates acting as crack nucleation sites. However, after too long milling times, here 24 h, the layers show a crack network. The pore size distributions do not indicate an increased capillary pressure as the cause. Furthermore, large agglomerates as nucleation points can be excluded. The explanatory hypothesis of this study attributes the inferior crack pattern to the considerable surface area of the numerous small particles and the ionomer distribution in the ink.

The numerous smaller particles have a greater specific surface area. With the x_{50} and the assumption of particles and agglomerates as nonporous spheres, for example, the specific surface area increases ninefold from 1 to 24 h of milling time. Free ionomer from the ink adsorbs onto the created particle surface. This is becoming increasingly difficult to procure and is no longer available in the form of a stress-adsorbing binder between particles when the film solidifies during the drying process. The cohesion of this layer and its resistance to cracking therefore diminish.

The crack resistance is re-improved by increasing the concentration of free ionomer. This is achieved by increasing the *I/C* ratio. The PSD and thus the surface area of the particles are similar after the same processing regardless of the *I/C* ratio. Nevertheless, with sufficient additional ionomer, low-crack layers reappear. It is postulated that the additional ionomer adsorbs to the previously uncovered particle surfaces, leaving the remainder as free ionomer in the ink and thus as a binder.

In conclusion, it can be stated that the ionomer distribution in the ink and the ionomer requirement for low-crack layers depend on the PSD of the inks. The static determination of the *I/C* ratio, regardless of the ink grinding process and thus the PSD, is inadequate. It is essential to consider the *I/C* ratio and PSD in their respective contexts.

The objective of this study was to examine the relationship between ink processing and the resulting PSD, as well as the relationship between PSD and the layer properties, including the crack area and the pore structure. No statements are made regarding the resulting electrode performance, which is the subject of further studies.

Author Contributions

Philipp Quarz: conceptualization (lead); data curation (lead); formal analysis (lead); investigation (lead); methodology (lead); validation (lead); visualization (lead); writing – original draft (lead); writing – review and editing (lead). **Nadine Zimmerer**: conceptualization (supporting); investigation (supporting); methodology (equal); writing – original draft (supporting). **Linus Janning**: conceptualization (supporting); data curation (supporting); methodology (supporting). **Anna-Maria Steck**: data curation (equal). **Philip Scharfer**: supervision (equal). **Wilhelm Schabel**: supervision (equal).

Acknowledgments

The authors would like to thank Vincent Kast for doing the pore size measurements and crack analysis and Julian Klemens for collegial input to this work. Furthermore, the authors want to thank August Gladik, Chiara Hoffstetter, Marek Hubka, Dennis Scinov, Angela Duhatschek, Nico Korell and Adrian Reyes Mayorga for their input to this work.

Open Access funding enabled and organized by Projekt DEAL.

Conflicts of Interest

The authors declare no conflicts of interest.

Data Availability Statement

The data that support the findings of this study are available from the corresponding author upon reasonable request.

Declaration of Generative AI and AI-assisted Technologies in the Writing Process

During the preparation of this work, the authors used DeepL (DeepL SE, Germany) to improve readability and clarity. The authors reviewed and edited the content after usage and take full responsibility for the content of the publication.

References

1. E. Carcadea, M. Varlam, A. Marinoiu, M. Raceanu, M. S. Ismail, and D. B. Ingham, "Influence of Catalyst Structure on PEM Fuel Cell Performance—A Numerical Investigation," *International Journal of Hydrogen Energy* 44 (2019): 12829–12841, https://doi.org/10.1016/j.ijhydene.2018.12.155.

2. A. Z. Weber, R. L. Borup, R. M. Darling, et al., "A Critical Review of Modeling Transport Phenomena in Polymer-Electrolyte Fuel Cells," *Journal of the Electrochemical Society*, 161 (2014): F1254–F1299, https://doi.org/10.1149/2.0751412jes.

3. S. Obut and E. Alper, "Numerical Assessment of Dependence of Polymer Electrolyte Membrane Fuel Cell Performance on Cathode Catalyst Layer Parameters," *Journal of Power Sources* 196 (2011): 1920–1931, https://doi.org/10.1016/j.jpowsour.2010.10.030.

4. G. Inoue and M. Kawase, "Understanding Formation Mechanism of Heterogeneous Porous Structure of Catalyst Layer in Polymer Electrolyte Fuel Cell," *International Journal of Hydrogen Energy* 41 (2016): 21352–21365, https://doi.org/10.1016/j.ijhydene.2016.08.029.

5. M. B. Dixit, B. A. Harkey, F. Shen, and K. B. Hatzell, "Catalyst Layer Ink Interactions That Affect Coatability," *Journal of the Electrochemical Society* 165 (2018): F264–F271, https://doi.org/10.1149/2.0191805jes.

6. C. Lei, F. Yang, N. Macauley, et al., "Impact of Catalyst Ink Dispersing Solvent on PEM Fuel Cell Performance and Durability," *Journal of the Electrochemical Society* 168 (2021): 044517, https://doi.org/10.1149/1945-7111/abf2b0.

7. N. Hasegawa, A. Kamiya, T. Matsunaga, N. Kitano, and M. Harada, "Analysis of Crack Formation during Fuel Cell Catalyst Ink Drying Process. Reduction of Catalyst Layer Cracking by Addition of High Boiling Point Solvent," *Colloids and Surfaces A* 628 (2021): 127153, https://doi.org/10.1016/j.colsurfa.2021.127153.

8. J. Park, M. Ulsh, and S. A. Mauger, "Solvent Absorption Rate of Perfluorosulphonic Acid Membranes towards Understanding Direct Coating Processes," *International Journal of Hydrogen Energy* 46 (2021): 30239–30245, https://doi.org/10.1016/j.ijhydene.2021.06.168.

9. P. Quarz, N. Zimmerer, A.-M. Steck, P. Scharfer, and W. Schabel, "Carbon Nanotubes (CNT) as an Additive towards Crack-Free Catalyst Coated Membranes (CCM)," *International Journal of Hydrogen Energy* 57 (2024): 789–797, https://doi.org/10.1016/j.ijhydene.2024.01.049.

10. C.-H. Song and J.-S. Park, "Effect of Dispersion Solvents in Catalyst Inks on the Performance and Durability of Catalyst Layers in Proton Exchange Membrane Fuel Cells," *Energies* 12 (2019): 549, https://doi.org/10.3390/en12030549.

11. T. Suzuki, R. Hashizume, and M. Hayase, "Effect of Blending Carbon Nanoparticles and Nanotubes on the Formation of Porous Structure and the Performance of Proton Exchange Membrane Fuel Cell," *Journal of Power Sources* 286 (2015): 109–117, https://doi.org/10.1016/j.jpowsour.2015.03.119.

12. S. Holdcroft, "Fuel Cell Catalyst Layers: A Polymer Science Perspective," *Chemistry of Materials* 26 (2014): 381–393, https://doi.org/10.1021/cm401445h.

13. A. Therdthianwong, P. Ekdharmasuit, and S. Therdthianwong, "Fabrication and Performance of Membrane Electrode Assembly Prepared by a Catalyst-Coated Membrane Method: Effect of Solvents Used in a Catalyst Ink Mixture," *Energy & Fuels* 24 (2010): 1191–1196, https://doi.org/10.1021/ef901105k.

14. S. H. Woo, S. Kim, S. Woo, et al., "Investigating the Effect of Solvent Composition on Ink Structure and Crack Formation in Polymer Electrolyte Membrane Fuel Cell Catalyst Layers," *The Korean Journal of Chemical Engineering* 40 (2023): 2455–2462, https://doi.org/10.1007/s11814-023-1474-3.

15. E. Hoffmann, S. Zhang, M. Thoma, C. Damm, and W. Peukert, "Formulation of Carbon Black-Ionomer Dispersions for Thin Film Formation in Fuel Cells," *Particuology* 44 (2019): 7–21, https://doi.org/10.1016/j.partic.2018.08.001.

16. P. Quarz, N. Zimmerer, L. Janning, F. Mannes, P. Scharfer, and W. Schabel, "From Decal Coating to Membrane Direct Coating in Catalyst Coated Membrane (CCM) Production," in Wasserstofftechnologien Effizient Produziert (Verlag Wissenschaftliche Scripten, 2024), 135–144, 1, https://doi.org/10.60687/2025-0065.

17. H. Liu, L. Ney, N. Zamel, and X. Li, "Effect of Catalyst Ink and Formation Process on the Multiscale Structure of Catalyst Layers in PEM Fuel Cells," *Applied Sciences* 12 (2022): 3776, https://doi.org/10.3390/app12083776.

18. C. M. Baez-Cotto, J. P. Pfeilsticker, A. O. Godoy, et al., "The Effect of Ink Ball Milling Time on Interparticle Interactions and Ink Microstructure and Their Influence on Crack Formation in Rod-Coated Catalyst Layers," *Journal of Power Sources* 583 (2023): 233567, https://doi.org/10.1016/j.jpowsour.2023.233567.

19. A. Lindermeir, G. Rosenthal, U. Kunz, and U. Hoffmann, "On the Question of MEA Preparation for DMFCs," *Journal of Power Sources* 129 (2004): 180–187, https://doi.org/10.1016/j.jpowsour.2003.11.002.

20. C. Liu, M. Luo, R. Zeis, et al., "Fabrication of Catalyst Layer for Proton Exchange Membrane Water Electrolyzer: I. Effects of Dispersion on Particle Size Distribution and Rheological Behavior," *International Journal of Hydrogen Energy* 52 (2024): 1143–1154, https://doi.org/10.1016/j.ijhydene.2023.08.154.

21. F. Scheepers, A. Stähler, M. Stähler, M. Carmo, W. Lehnert, and D. Stolten, "Layer Formation from Polymer Carbon-Black Dispersions," *Coatings* 8 (2018): 450, https://doi.org/10.3390/coatings8120450.

22. P. Quarz, N. Zimmerer, P. Scharfer, and W. Schabel, "About Drying Phenomena of Fuel Cell and Electrolyzer CCM Inks: Selectivity of the Evaporation of 1-Propanol/Water Mixtures," *Fuel Cells* 24 (2024): 108–121, https://doi.org/10.1002/fuce.202300252.

23. N. Zimmerer, P. Quarz, E. Terhorst, L. Janning, P. Scharfer, and W. Schabel, "Influence of Ink Formulation and Drying Parameters on Component Composition during Drying of Catalyst Layers for Polymer Electrolyte Membrane Fuel Cells and Electrolyzers," *Energy Technology* (2025): 2500516, https://doi.org/10.1002/ente.202500516.

24. M. Yamamura, "Manipulating Cracks with Selective Drying in Binary Solvent Mixture Suspensions," *Journal of Chemical Engineering of Japan* 58 (2025): 2545622, https://doi.org/10.1080/00219592.2025.2545622.

25. F. Scheepers, A. Stähler, M. Stähler, M. Carmo, W. Lehnert, and D. Stolten, "Steering and in Situ Monitoring of Drying Phenomena during Film Fabrication," *Journal of Coatings Technology and Research* 16 (2019): 1213–1221, https://doi.org/10.1007/s11998-019-00206-5.

26. J. Park, Z. Kang, G. Bender, M. Ulsh, and S. A. Mauger, "Roll-to-Roll Production of Catalyst Coated Membranes for Low-Temperature Electrolyzers," *Journal of Power Sources* 479 (2020): 228819, https://doi.org/10.1016/j.jpowsour.2020.228819.

27. Q. Gong, C. Li, Y. Liu, et al., "Effects of Ink Formulation on Construction of Catalyst Layers for High-Performance Polymer Electrolyte Membrane Fuel Cells," *ACS Applied Materials & Interfaces* 13 (2021): 37004–37013, https://doi.org/10.1021/acsami.1c06711.

28. M. Lee, M. Uchida, H. Yano, D. A. Tryk, H. Uchida, and M. Watanabe, "New Evaluation Method for the Effectiveness of Platinum/Carbon Electrocatalysts under Operating Conditions," *Electrochimica Acta* 55 (2010): 8504–8512, https://doi.org/10.1016/j.electacta.2010.07.071.

29. J. Xie, F. Xu, D. L. Wood, K. L. More, T. A. Zawodzinski, and W. H. Smith, "Influence of Ionomer Content on the Structure and Performance of PEFC Membrane Electrode Assemblies," *Electrochimica Acta* 55 (2010): 7404–7412, https://doi.org/10.1016/j.electacta.2010.06.067.

30. H. Yu, J. M. Roller, W. E. Mustain, and R. Maric, "Influence of the Ionomer/Carbon Ratio for Low-Pt Loading Catalyst Layer Prepared by Reactive Spray Deposition Technology," *Journal of Power Sources* 283 (2015): 84–94, https://doi.org/10.1016/j.jpowsour.2015.02.101.

31. S. Shukla, S. Bhattacharjee, A. Z. Weber, and M. Secanell, "Experimental and Theoretical Analysis of Ink Dispersion Stability for Polymer Electrolyte Fuel Cell Applications," *Journal of the Electrochemical Society* 164 (2017): 600–609, https://doi.org/10.1149/2.0961706jes.

32. S. Khandavalli, J. H. Park, N. N. Kariuki, et al., "Rheological Investigation on the Microstructure of Fuel Cell Catalyst Inks," *ACS Applied Materials & Interfaces* 10 (2018): 43610–43622, https://doi.org/10.1021/acsami.8b15039.

33. V. Berejnov, D. Susac, J. Stumper, and A. P. Hitchcock, "3D Chemical Mapping of PEM Fuel Cell Cathodes by Scanning Transmission Soft X-Ray SpectroTomography," *ECS Transactions* 50 (2013): 361–368, https://doi.org/10.1149/05002.0361ecst.

34. M. Lopez-Haro, L. Guétaz, T. Printemps, et al., "Three-Dimensional Analysis of Nafion Layers in Fuel Cell Electrodes," *Nature Communications* 5 (2014): 5229, https://doi.org/10.1038/ncomms6229.

35. N. Kumano, K. Kudo, Y. Akimoto, M. Ishii, and H. Nakamura, "Influence of Ionomer Adsorption on Agglomerate Structures in High-Solid Catalyst Inks," *Carbon* 169 (2020): 429–439, https://doi.org/10.1016/j.carbon.2020.07.047.

36. N. Kumano, K. Kudo, A. Suda, Y. Akimoto, M. Ishii, and H. Nakamura, "Controlling Cracking Formation in Fuel Cell Catalyst Layers," *Journal of Power Sources* 419 (2019): 219–228, https://doi.org/10.1016/j.jpowsour.2019.02.058.

37. E. Middelman, "Improved PEM Fuel Cell Electrodes by Controlled Self-Assembly," *Fuel Cells Bulletin* 2002 (2002): 9–12, https://doi.org/10.1016/S1464-2859(02)11028-5.

38. S. Takahashi, T. Mashio, N. Horibe, K. Akizuki, and A. Ohma, "Analysis of the Microstructure Formation Process and Its Influence on the Performance of Polymer Electrolyte Fuel-Cell Catalyst Layers,"

ChemElectroChem 2 (2015): 1560–1567, https://doi.org/10.1002/celc.201500131.

39. S.-H. Lee, S. H. Woo, B. J. Pak, et al., "Ink Droplet Drying Analysis for Understanding the Ink-Catalyst Layer Transition in Proton Exchange Membrane Fuel Cells," *Journal of Power Sources* 585 (2023): 233644, https://doi.org/10.1016/j.jpowsour.2023.233644.

40. S. Du, S. Guan, S. Mehrazi, et al., "Effect of Dispersion Method and Catalyst on the Crack Morphology and Performance of Catalyst Layer of PEMFC," *Journal of the Electrochemical Society* 168 (2021): 114506, https://doi.org/10.1149/1945-7111/ac3598.

41. S. Li, J. Yuan, G. Xie, and B. Sundén, "Effects of Agglomerate Model Parameters on Transport Characterization and Performance of PEM Fuel Cells," *International Journal of Hydrogen Energy* 43 (2018): 8451–8463, https://doi.org/10.1016/j.ijhydene.2018.03.106.

42. R. Gordon, M. Kassar, and N. Willenbacher, "Effect of Polymeric Binders on Dispersion of Active Particles in Aqueous $LiFePO_4$-Based Cathode Slurries as Well as on Mechanical and Electrical Properties of Corresponding Dry Layers," *ACS Omega* 5 (2020): 11455–11465, https://doi.org/10.1021/acsomega.0c00477.

43. L. Karásek and M. Sumita, "Characterization of Dispersion State of Filler and Polymer-Filler Interactions in Rubber-Carbon Black Composites," *Journal of Materials Science* 31 (1996): 281–289, https://doi.org/10.1007/BF01139141.

44. G. Kaysan, R. Kräling, M. Meier, H. Nirschl, G. Guthausen, and M. Kind, "Investigation of the Surfactant Distribution in Oil-in-Water Emulsions during the Crystallization of the Dispersed Phase via Nuclear Magnetic Resonance Relaxometry and Diffusometry," *Magnetic Resonance in Chemistry* 60 (2022): 1131–1147, https://doi.org/10.1002/mrc.5305.

45. A. Jankovic, "Variables Affecting the Fine Grinding of Minerals Using Stirred Mills," *Minerals Engineering* 16 (2003): 337–345, https://doi.org/10.1016/S0892-6875(03)00007-4.

46. H. Shin, S. Lee, H. Suk Jung, and J.-B. Kim, "Effect of Ball Size and Powder Loading on the Milling Efficiency of a Laboratory-Scale Wet Ball Mill," *Ceramics International* 39 (2013): 8963–8968, https://doi.org/10.1016/j.ceramint.2013.04.093.

47. A. Kwade and J. Schwedes, "Breaking Characteristics of Different Materials and Their Effect on Stress Intensity and Stress Number in Stirred Media Mills," *Powder Technology* 122 (2002): 109–121, https://doi.org/10.1016/S0032-5910(01)00406-5.

48. L. M. Arya and J. L. Heitman, "A Non-Empirical Method for Computing Pore Radii and Soil Water Characteristics from Particle-Size Distribution," *Soil Science Society of America Journal* 79 (2015): 1537–1544, https://doi.org/10.2136/sssaj2015.04.0145.

49. M. Wang, J. H. Park, S. Kabir, et al., "Impact of Catalyst Ink Dispersing Methodology on Fuel Cell Performance Using in-Situ X-Ray Scattering," *ACS Applied Energy Materials* 2 (2019): 6417–6427, https://doi.org/10.1021/acsaem.9b01037.

50. M. P. Manahan, S. Kim, E. C. Kumbur, and M. M. Mench, "Effects of Surface Irregularities and Interfacial Cracks on Polymer Electrolyte Fuel Cell Performance," *ECS Transactions* 25 (2009): 1745–1754, https://doi.org/10.1149/1.3210730.

51. H. Markötter, J. Haußmann, R. Alink, et al., "Influence of Cracks in the Microporous Layer on the Water Distribution in a PEM Fuel Cell Investigated by Synchrotron Radiography," *Electrochemistry Communications* 34 (2013): 22–24, https://doi.org/10.1016/j.elecom.2013.04.006.

52. M.-A. Goulet, S. Arbour, M. Lauritzen, and E. Kjeang, "Water Sorption and Expansion of an Ionomer Membrane Constrained by Fuel Cell Electrodes," *Journal of Power Sources* 274 (2015): 94–100, https://doi.org/10.1016/j.jpowsour.2014.10.040.

53. Y. Singh, R. M. H. Khorasany, W. H. J. Kim, et al., "Ex Situ Characterization and Modelling of Fatigue Crack Propagation in Catalyst Coated Membrane Composites for Fuel Cell Applications," *International Journal of Hydrogen Energy* 44 (2019): 12057–12072, https://doi.org/10.1016/j.ijhydene.2019.03.108.

54. G. Ding, M. H. Santare, A. M. Karlsson, and A. Kusoglu, "Numerical Evaluation of Crack Growth in Polymer Electrolyte Fuel Cell Membranes Based on Plastically Dissipated Energy," *Journal of Power Sources* 316 (2016): 114–123, https://doi.org/10.1016/j.jpowsour.2016.03.031.

55. S. Kundu, M. W. Fowler, L. C. Simon, and S. Grot, "Morphological Features (defects) in Fuel Cell Membrane Electrode Assemblies," *Journal of Power Sources* 157 (2006): 650–656, https://doi.org/10.1016/j.jpowsour.2005.12.027.

56. A. Phillips, M. Ulsh, K. C. Neyerlin, J. Porter, and G. Bender, "Impacts of Electrode Coating Irregularities on Polymer Electrolyte Membrane Fuel Cell Lifetime Using Quasi in-Situ Infrared Thermography and Accelerated Stress Testing," *International Journal of Hydrogen Energy* 43 (2018): 6390–6399, https://doi.org/10.1016/j.ijhydene.2018.02.050.

57. G. W. Scherer, "Theory of Drying," *Journal of the American Ceramic Society* 73 (1990): 3–14, https://doi.org/10.1111/j.1151-2916.1990.tb05082.x.

58. K. B. Singh and M. S. Tirumkudulu, "Cracking in Drying Colloidal Films," *Physical Review Letters* 98 (2007): 218302, https://doi.org/10.1103/PhysRevLett.98.218302.

59. M. S. Tirumkudulu and W. B. Russel, "Cracking in Drying Latex Films," *Langmuir* 21 (2005): 4938–4948, https://doi.org/10.1021/la048298k.

60. K. B. Singh, G. Deoghare, and M. S. Tirumkudulu, "Cracking in Soft-Hard Latex Blends: Theory and Experiments," *Langmuir* 25 (2009): 751–760, https://doi.org/10.1021/la802857q.

61. R. C. Chiu, T. J. Garino, and M. J. Cima, "Drying of Granular Ceramic Films: I, Effect of Processing Variables on Cracking Behavior," *Journal of the American Ceramic Society* 76 (1993): 2257–2264, https://doi.org/10.1111/j.1151-2916.1993.tb07762.x.

62. Y. Wu and L. F. Francis, "Effect of Particle Size Distribution on Stress Development and Microstructure of Particulate Coatings," *Journal of Coatings Technology and Research* 14 (2017): 455–465, https://doi.org/10.1007/s11998-016-9866-5.

63. T. Kanai and T. Sawada, "New Route to Produce Dry Colloidal Crystals without Cracks," *Langmuir* 25 (2009): 13315–13317, https://doi.org/10.1021/la9033854.

64. T. Mabuchi, S.-F. Huang, and T. Tokumasu, "Dispersion of Nafion Ionomer Aggregates in 1-Propanol/Water Solutions: Effects of Ionomer Concentration, Alcohol Content, and Salt Addition," *Macromolecules* 53 (2020): 3273–3283, https://doi.org/10.1021/acs.macromol.9b02725.

65. F. Löffler and J. Raasch, Grundlagen der Mechanischen Verfahrenstechnik (Vieweg, 1992).

66. S. M. Andersen, M. Borghei, R. Dhiman, V. Ruiz, E. Kauppinen, and E. Skou, "Adsorption Behavior of Perfluorinated Sulfonic Acid Ionomer on Highly Graphitized Carbon Nanofibers and Their Thermal Stabilities," *The Journal of Physical Chemistry C* 118 (2014): 10814–10823, https://doi.org/10.1021/jp501088d.

Supporting Information

Supporting Information is available from the Wiley Online Library or from the author. **Supporting Fig. 1:** Initial catalyst powder with agglomerate sizes up to ≈80 µm. **Supporting Fig. 2:** Cumulative PSD depending on the milling time t from t = 1, 3, 6, and 24 h in a ball mill. In addition, the PSD of the catalyst powder in the solvent mixture without further processing (t = 0 h) is shown. **Supporting Fig. 3:** Agglomerates (circled in red) as common nucleation point for cracks, independent on the milling time of the inks. The number and size of the agglomerates shown are not representative of the inks themselves, but rather serve to illustrate their general appearance. **Supporting Fig. 4:** PSDs (points) of the inks

compared to the pore diameter distributions -dV/dlog(dp) (bars) of the formed layers after 1, 3, 6, and 24 h of ink processing. Shape and qualitative sizes of particles and pores match together for each ink. X-axis represents the pore diameter dp respective the particle size x. **Supporting Fig. 5:** Varying sizes of secondary pores between two (I) primary particles, (II) aggregates and (III) agglomerates. In addition, primary pores occur in aggregates and agglomerates. These are larger in agglomerates. **Supporting Fig. 6:** Influence of the I/C ratio on pore diameter distribution. **Supporting Fig. 7:** Crack pattern depending on the I/C ratio for inks processed for 3 and 24 h. **Supporting Fig. 8:** Influence of the I/C ratio on crack pattern and defect area fraction for inks processed for 3 and 24 h.